InSAR observations of aseismic slip associated with an earthquake swarm in the Columbia River flood basalts

Charles Wicks,[1] Weston Thelen,[2,3] Craig Weaver,[4] Joan Gomberg,[4] Alan Rohay,[5] and Paul Bodin[2]

Received 8 April 2011; revised 28 July 2011; accepted 1 October 2011; published 10 December 2011.

[1] In 2009 a swarm of small shallow earthquakes occurred within the basalt flows of the Columbia River Basalt Group (CRBG). The swarm occurred within a dense seismic network in the U.S. Department of Energy's Hanford Site. Data from the seismic network along with interferometric synthetic aperture radar (InSAR) data from the European Space Agency's (ESA) ENVISAT satellite provide insight into the nature of the swarm. By modeling the InSAR deformation data we constructed a model that consists of a shallow thrust fault and a near horizontal fault. We suggest that the near horizontal lying fault is a bedding-plane fault located between basalt flows. The geodetic moment of the modeled fault system is about eight times the cumulative seismic moment of the swarm. Precise location estimates of the swarm earthquakes indicate that the area of highest slip on the thrust fault, ~70 mm of slip less than ~0.5 km depth, was not located within the swarm cluster. Most of the slip on the faults appears to have progressed aseismically and we suggest that interbed sediments play a central role in the slip process.

Citation: Wicks, C., W. Thelen, C. Weaver, J. Gomberg, A. Rohay, and P. Bodin (2011), InSAR observations of aseismic slip associated with an earthquake swarm in the Columbia River flood basalts, *J. Geophys. Res.*, *116*, B12304, doi:10.1029/2011JB008433.

1. Introduction

[2] The flood basalts of the CRBG form the Columbia Basin located in southeastern Washington, northeastern Oregon and part of western Idaho. The most seismically active sub-province of the Columbia Basin is the Yakima Fold Belt (YFB) in central-southern Washington. The YFB, characterized by anticlinal ridges separated by broad synclinal valleys [*Reidel et al.*, 1989], is an area of ~1 mm yr^{-1} near N-S convergence [*Wells and Simpson*, 2001], ongoing subsidence, and the thickest accumulation of CRBG (~4 km) [*Reidel et al.*, 1989]. Shallow (less than ~2 km depth) swarms of micro-earthquakes were first detected nearly 40 years ago in and around the Hanford Nuclear Site located in the eastern YFB [*Pitt*, 1971; *Malone et al.*, 1975] (Figure 1). The Wooded Island area of Hanford has been a source of persistent seismic swarm activity, with a major swarm occurring in 1969–1970 (Figure 2), and minor activity in 1975 and 1988. The most recent swarm commenced abruptly in January 2009, all of the ~1500 swarm earthquakes had a magnitude of 3 or less, and the earthquakes were shallow (mostly less than 1 km depth). The largest earthquakes in the swarm produced accelerations as high as 0.15 g, and the magnitude-equivalent cumulative moment of the swarm is M 4.0. This is the first recorded swarm in the Columbia Basin for which geodetic measurements of surface deformation are available and precise earthquake relocation is possible. The earthquake magnitude-frequency distribution results in a b-value for the swarm of 1.1, suggesting pervasive fracturing or the presence of fluids [*Mogi*, 1967].

2. InSAR Data and Modeling

[3] InSAR deformation measurements, shown in the interferograms (Figure 2 and Table 1), reveal a distinct two-peaked ~2 km long area of deformation with low amplitude range change (~35 mm peak amplitude). The deforming area is spatially and temporally coincident with the earthquake swarm (Figures 2 and 3). Data from five interferograms are shown in this study (Figures 2 and 3 and Table 1). The deformation cross sections along A-A' (Figures 2 and 3b) show the time evolution of the deformation field relative to the evolution of seismicity (Figure 3a).

[4] To estimate the sources of deformation, we model the deformation fields in interferograms three and four (Figures 2 and 3b and Table 1). These two interferograms span the detected surface deformation (Figures 2 and 3) for this episode and they also sample nearly the same time interval (Figure 3 and Table 1). Interferogram three is calculated from data collected during descending satellite

[1]U. S. Geological Survey, Menlo Park, California, USA.
[2]Pacific Northwest Seismic Network, University of Washington, Seattle, Washington, USA.
[3]Now at U. S. Geological Survey, Cascades Volcano Observatory, Vancouver, Washington, USA.
[4]U. S. Geological Survey at Department of Earth and Space Sciences, University of Washington, Seattle, Washington, USA.
[5]Environmental Characterization and Risk Assessment Group, Pacific Northwest National Laboratory, Richland, Washington, USA.

Copyright 2011 by the American Geophysical Union.
0148-0227/11/2011JB008433

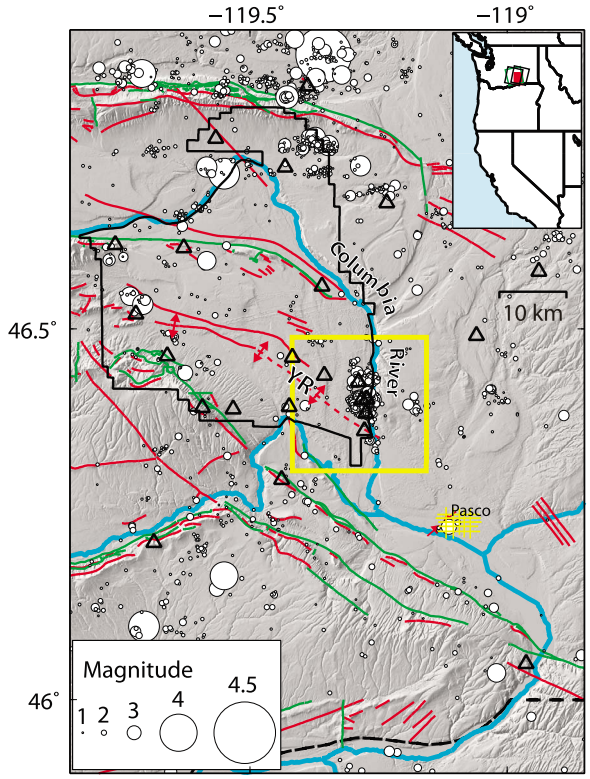

Figure 1. Reference map for earthquake swarm area with shaded relief background. A regional location map is inset in the upper right where the red square marks the location of the reference map and the tilted boxes represent the radar scenes (Table 1) used in this study (Track 342 is the left black box, Track 70 is the right black box, and Track 77 is the green box). Earthquakes with a coda magnitude (Mc) 1.0 and larger in the University of Washington's Pacific Northwest Seismic Network earthquake catalog from 1 January 1969 through 29 January 2010 are marked with white filled circles. Major rivers are cyan lines (the Columbia River is labeled), undifferentiated faults are green, undifferentiated fold axes are red—the Yakima Ridge Anticline (labeled YR, and dashed where recently extended by *Blakely et al.* [2011] is marked with outward directed arrows. The Hanford Site boundary is a solid black line, the broken black line is the Oregon Washington border. The locations of seismic stations used in this study are marked with black triangles. The detailed study area of the swarm (the area shown in Figure 2) is inside the yellow box.

trajectories, whereas interferogram four is calculated from data collected during ascending trajectories. The shape and sign of the SW deformation peak are diagnostic of a reverse fault that dips to the NE and strikes NW-SE (Figures 2 and 3b). The higher amplitude for the two peaks on interferogram four indicates a component of horizontal movement directed toward the satellite in the ascending mode of interferogram four and away from the satellite in the descending mode of interferogram three.

[5] To model the interferograms, we first resampled the InSAR data using a quadtree algorithm thus reducing the large number of highly correlated data points in each InSAR image [*Jónsson et al.*, 2002; *Simons et al.*, 2002] (Figures 4a and 4b). Allowing for shear dislocations in an elastic half-space, we conducted preliminary exploratory modeling of the data using first one then two rectangular sources of uniform slip [*Okada*, 1985]. The addition of the second source dramatically reduced the variance of the residual compared to one source, so we allowed two sources of distributed slip in our modeling procedure. We then investigated the data with a model that consists of two independent patches of distributed slip, within a homogenous elastic half-space. Each slip distribution is described functionally by a two-dimensional Weibull distribution that includes a co-variance (or interaction) parameter [*Myrhaug and Rue*, 1998; *Brodtkorb et al.*, 2000]. We use a constrained Monte Carlo nonlinear least squares inversion scheme to find the location, strike, dip, three components of slip, Weibull parameters for each slip distribution, and include tilt and static shift parameters for each interferogram. This method minimizes the variance of the residual, where the residual is defined as the difference between the equally weighted quadtree data and the calculated values. This method allows us to search a wide range of model geometries and slip distributions automatically, and it also enables automatic modeling of sharp spatial discontinuities in the deformation field.

[6] The two distributed-slip sources that best fit the data are a shallow thrust fault and a near-horizontal lying fault at about 0.5 km depth (Figure 5). The shallow thrust fault is the best constrained of the two sources, with depth to the top of the fault between 0.1 and 0.25 km and dip between 25 and 50 degrees to the NE. The depth of the near horizontal lying fault is between 0.2 and 1 km and the dip is between 25 degrees to the SW and 30 degrees to the NE. We need additional information to help constrain the geometry of the near-horizontal lying fault. There is no surface expression of faulting in the area probably because giant Pleistocene flooding events [*Bretz*, 1925; *Waitt*, 1980] have scoured and buried the surface in the swarm area [*Reidel et al.*, 1992], effectively concealing possible fault scarps older than about 11 ka. We favor a horizontal bedding-plane fault for two main reasons: (1) The main structural weakness in the local CRBG basalts are along the contacts between basalt flows, especially those with interflow sediments, and the flows appear to be dipping less than ~1 degree to the north and south (from well data for wells DDH-3, DC-15 and DB-1 in Figure 2); and (2) stress coupling between a shallow thrust fault and bedding-plane fault in a stratified medium subjected to horizontal compression has been demonstrated in numerical experiments [*Cooke and Pollard*, 1997]. Bedding-plane slip during thrust fault earthquakes has also been observed in nature [*Philip and Meghraoui*, 1983; *Yeats et al.*, 1997]. So, we constrain the near-horizontal lying fault to be a bedding-plane fault with zero degrees dip and show the resulting model in Figure 5. This model has the form of a listric fault, but we have not explored variable curvature.

[7] The fit of the final model to the data is good—the variance of the residual is about 4 mm^2 (Figures 4c and 4d), which is consistent with the variance of the noise outside the deforming area. Our estimate of the model parameters for the model shown in Figure 5 accounts for 95% of the variance in the data. This parameterization implies a uniform slip direction across each separate slip distribution. Because the fit to the data was good, we were not compelled to

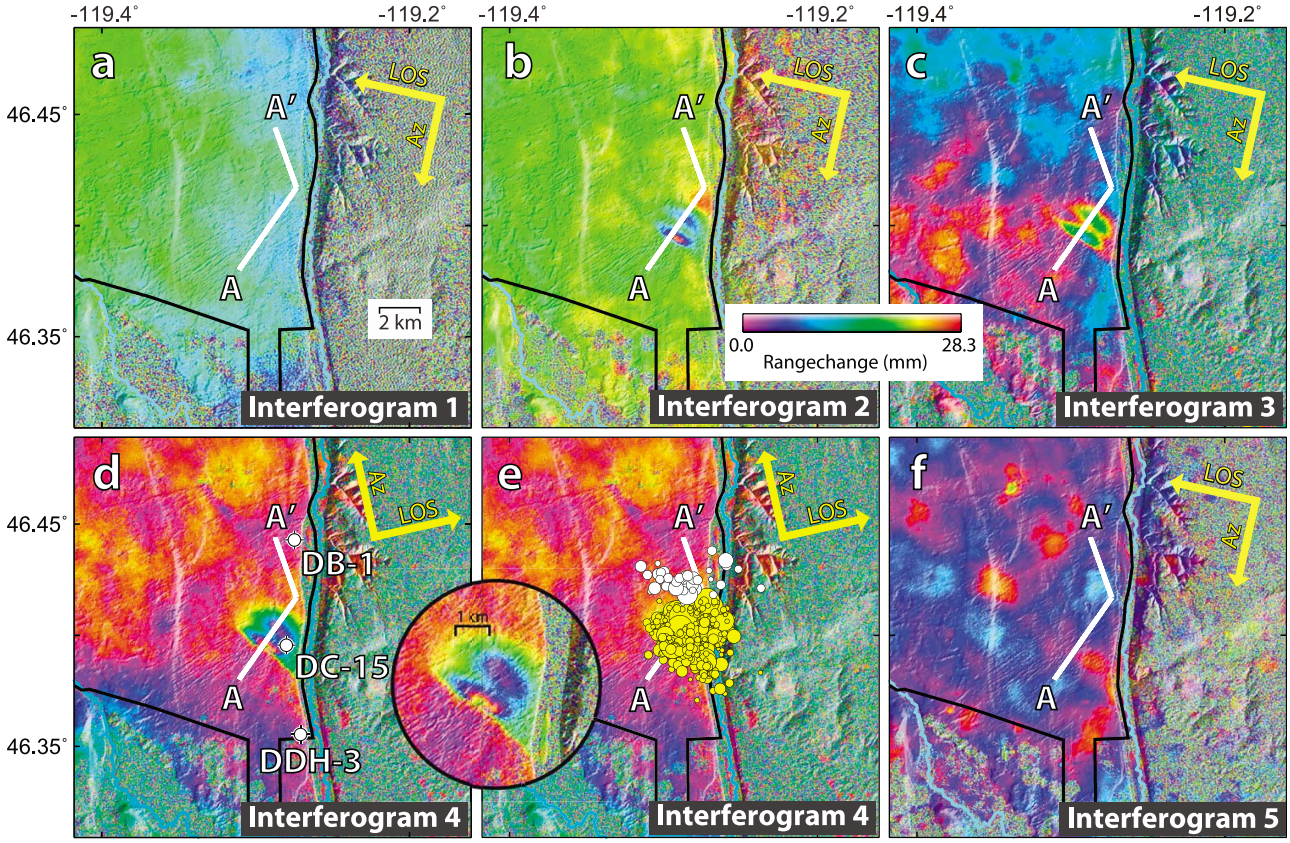

Figure 2. Five ENVISAT interferograms used in this study (Table 1). The line-of-sight (LOS) look direction from the satellite to the ground is shown with a yellow arrow labeled "LOS." The flight direction of the satellite is given with a yellow arrow labeled "Az." Colors refer to the range change (change in distance from a point on the ground to the satellite) as given in the color scale. The white line shows the location of cross-section A-A' in Figure 3. The bold black line is the Harford Site boundary and the near N-S irregular cyan line shows the location of the Columbia River. The areas of incoherence (mostly east of the Columbia River) are from agricultural activity. (a) Interferogram number one. (b) Interferogram number two. (c) Interferogram number three. (d) Interferogram number four. The round inset shows an unobstructed magnified view of the deformation field. Three wells, discussed in the text, are labeled DDH-3, DC-15, and DB-1. (e) Same as Figure 2d with earthquake locations from 2009 in yellow, and earthquake locations from the 1969–1971 Wooded Island earthquake swarm [*Pitt*, 1971] in white. Although the 1969–1971 swarm plots to the north of the 2009 swarm, the much sparser seismic network used to locate the early swarm casts doubt on any separation between the two swarms. (f) Interferogram number five.

introduce further complexity to the parameterization. Uncertainties (95%) in model parameters, and rejection of candidate models discussed were found by means of an F test. *Jónsson* [2002] showed that the quadtree parsed data can be treated as independent giving us some justification in the use of this method of uncertainty estimation.

[8] Slip on the thrust fault is concentrated on the updip end of the fault where the modeled slip occurred without accompanying seismicity (Figure 5). The depth to the top of the thrust fault could be so shallow as to reach the top of the basalt (~0.1 km depth). Because no seismicity is associated with the shallow slip on the thrust fault, we conclude that it is an existing feature that has very low

Table 1. Parameters for ENVISAT Radar Scenes Used in Study[a]

Interferogram Number	Master Scene Date	Slave Scene Date	Track	Flight Direction	$B_\perp$ (m)
1	2008/07/24	2009/02/19	342	Descending	183
2	2009/02/19	2009/04/30	342	Descending	44
3	2008/05/31	2009/07/25	70	Descending	38
4	2009/06/01	2009/07/26	77	Ascending	132
5	2009/07/25	2009/10/03	70	Descending	210

[a]Interferogram numbers are used in Figures 2, 3, and 4. $B_\perp$ is the perpendicular baseline separation between the two satellite orbits during master and slave image acquisition.

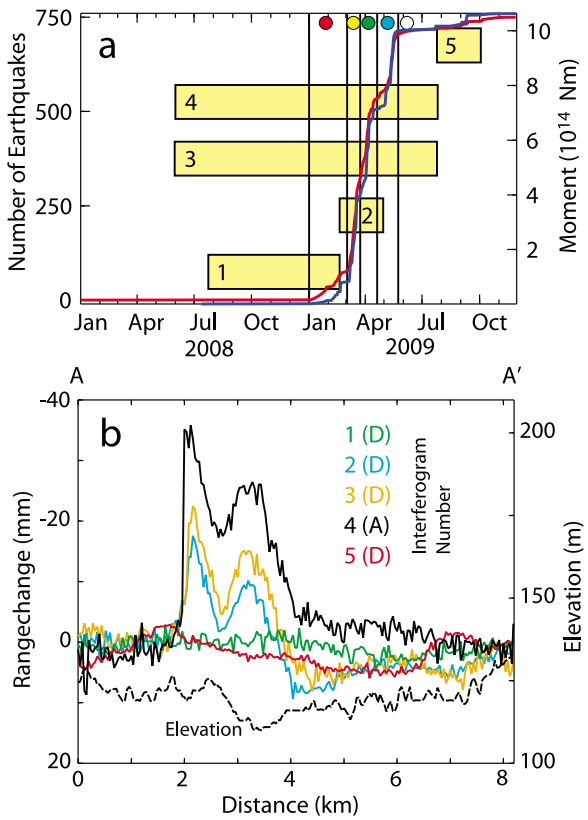

Figure 3. Time evolution of earthquake swarm and deformation profiles. (a) A plot of cumulative seismicity (red line) and cumulative moment (blue line) for earthquakes magnitude 1.0 and larger shows the time development of the micro-earthquake swarm. The yellow boxes show the time span covered by each interferogram, with interferogram index number (Figure 2 and Table 1). The vertical lines break the swarm into time segments to show the migration of seismicity in Figure 5; the filled circle at the top of each time segment corresponds to the color used to plot the earthquake locations in Figure 5. (b) Deformation profiles (solid lines) for the five interferograms along A-A' (Figure 2 and Table 1). The color of each profile indicates the interferogram number in Figures 2 and 3a. The black dashed line on the bottom shows the elevation profile along A-A'. The letters in parentheses after each interferogram number indicate whether it is ascending (A) or descending (D).

shear strength. We cannot determine the depth extent of the thrust fault; within 95% uncertainty a fault that bottoms at 1.1 km depth fits the data as well as one that bottoms at 4 km depth, the bottom of the basalts. The thrust fault shown, which bottoms at about 1.1 km depth, is the shortest fault possible without a significant degradation to the data fit. Although the model shows more slip on the thrust fault than on the bedding-plane fault, at the 95% uncertainty level we cannot say the slip on one fault is larger than on the other.

[9] The in-plane slip on the bedding-plane fault is directed toward the thrust fault. Slip on the bedding-plane fault alone is equivalent to a M 4.37 earthquake and the underlying swarm is equivalent to a M 4.0 earthquake, so the modeled bedding-plane fault is unlikely to be a simple ersatz deformation source for the more complex underlying swarm source—the largest earthquakes display a variety of fault mechanisms. Because the bedding plane fault extends into an area without InSAR data, we investigated the possibility of a more compact slip patch on the bedding plane by forcing the length of the fault to the shortest value possible without significant degradation to the fit (95% probability). This compact bedding-plane fault extends only slightly east of the Columbia River. The geodetic magnitude of the compact bedding-plane fault is M 4.31, still significantly larger than the underlying swarm magnitude. The combined geodetic magnitude of the two model faults in Figure 5 is about M 4.5.

3. Earthquake Relocation and Migration

[10] Knowledge of the slip history on the faults could give some insight as to the causative physical processes at work in the subsurface. Temporally, however, the InSAR data offers only a few details on the slip history (Figures 2 and 3). The deformation profiles in Figure 3b show that the slip on both faults did not occur in one brief pulse. The profiles for interferograms two and three (from descending orbits) are similar in form but the amplitudes of the two deformation peaks are larger in interferogram three. This indicates that both faults were slipping by the end of April 2009 and that they continued to slip probably until near the end of May 2009 (Figure 3a). We assume that the slip and the process or processes causing the slip led to a stress (or pressure) front that can be tracked by the earthquake rate [*Beeler and Lockner*, 2003]. Toward that end, we take a detailed look at the patterns of seismicity in the earthquake swarm.

[11] Independent from the deformation modeling, to improve the Pacific Northwest Seismic Network (PNSN) network locations, we employed phase differences and cross-correlation derived lags in a high-precision relocation using the program hypoDD [*Waldhauser and Ellsworth*, 2000]. We chose a subset of events for which there was a dense network configuration and required picks on 4 out of 5 stations within 5 km of the hypocenter to ensure a consistent station geometry. Many possible sources of error exist in the hypoDD locations including starting location, changing station configuration and mis-picked phases. In our case, the most error is introduced by variations in station distribution for different earthquakes. By systematically dropping stations in a jackknife test, similar to *Waldhauser and Ellsworth* [2000], we have estimated error ellipses within which 95% of the jackknife locations fall. These error ellipses have dimensions of 50 m horizontally and 70 m vertically, though the average errors are less than 20 m. These errors are consistent across different weighting schemes. By calculating the range of times of p- and s-wave arrivals at a pair of stations for common events we may bracket the range of derivative locations, assuming the earthquakes are part of the same swarm. When comparing the time differences on many stations of the full catalog with the hypoDD relocated earthquakes, we find that the range of time differences is the same, meaning that the locations for the whole swarm are contained within the cloud of hypoDD relocated earthquakes.

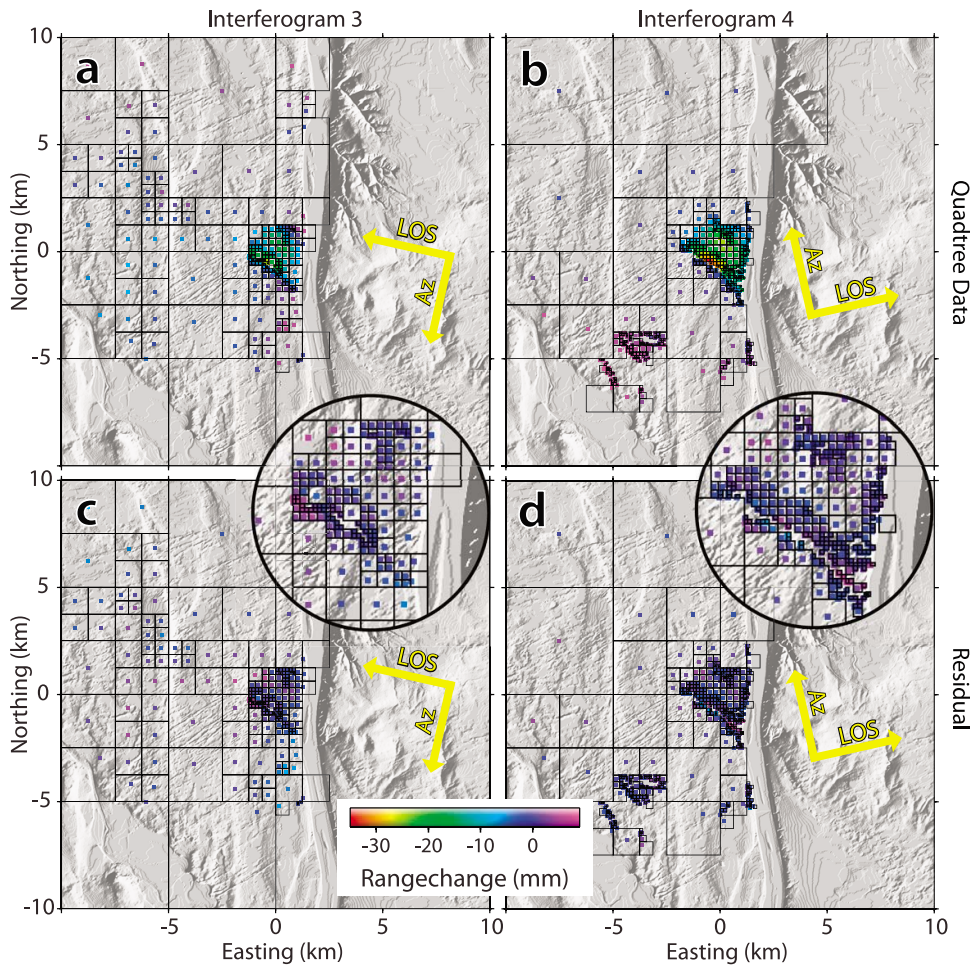

Figure 4. Quadtree parsed interferogram data (from Figure 2) used in modeling. The color scale at the bottom shows the mapping of color to range change. The yellow arrows are described in Figure 2. The black boxes show each quadtree window. (a) Quadtree data from Interferogram three (Figure 2 and Table 1). (b) Quadtree data from interferogram four (Figure 2 and Table 1). (c) Residual misfit for interferogram three data shown in Figure 4a (observed range change minus calculated) for the model shown in Figure 5. (d) Residual misfit for Interferogram four data shown in Figure 4b for the model shown in Figure 5.

[12] We attempt to extend the relocations to periods outside the period of time when the densest constellation of stations existed by comparing the waveforms of relocated earthquakes with those that were not relocated on common stations. If we assume that earthquakes with common waveforms have similar locations, then we may use this waveform matching to located events outside the time period of the best constellation of stations. A similar method was used by *Peng and Zhao* [2009] to relocate aftershocks of the 2004 Parkfield earthquake. We define two similar events as having maximum cross-correlation coefficients of 0.7 on 1.28 s windows around the p-wave arrival on three different stations. Through waveform matching, we are able to provide locations for two-thirds of the earthquakes (933) during time periods throughout the duration of the swarm. The resulting precise locations (Figures 5 and 6) show three main features: (1) The swarm is bounded by the two modeled faults, (2) the seismicity migrated from the NE to the SW, toward the shallow thrust fault (Figures 5 and 6), and (3) the seismic activity expanded in what appears to have been a diffusive process in updip and along strike directions (Figure 6).

4. Discussion

[13] As shown in a compilation by *Roland and McGuire* [2009], the migration of seismicity driven by aseismic slip has been observed to propagate at speeds on the order of km hr^{-1}, whereas the migration of seismicity driven by fluid pore pressure diffusion propagates at speeds on the order of m hr^{-1}. In the limited number of studies where the rupture speed of the aseismic slip accompanying a swarm has been observed geodetically [e.g., *Lohman and McGuire*, 2007] the aseismic slip has also been observed to propagate at speeds of km hr^{-1}. In Figure 6 we show that seismicity migrated in the swarm at rates of $\sim$1 m hr^{-1}, and spread in a manner consistent with fluid diffusion through low-permeability crustal rocks [*Roland and McGuire*, 2009]. Within the slow migration of hypocenters are vertical streaks, which indicate migration rates in excess of 100 m hr^{-1}, consistent with the

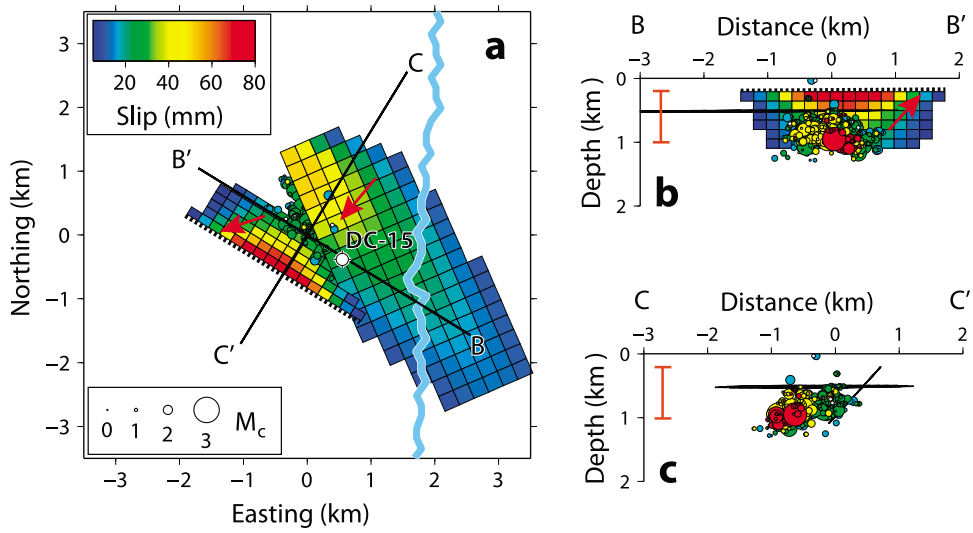

Figure 5. Modeled deformation sources. Three views of the modeled deformation sources derived from the InSAR data. The relocated earthquake locations are shown with circles that have a fill color corresponding to the time segments in Figure 3a. The black dashed line marks the top of the thrust fault. The thrust fault dips ~44° to the NE and the bedding-plane fault is constrained to have zero degrees dip. The red arrows show the in-plane slip direction for each fault. (a) A map view of the two deformation sources. Colors on the fault plane show the total slip in each panel. The earthquake magnitude scale is also the same for each panel. The labeled black lines show the locations of the cross-sections in Figures 5b and 5c. The location of the well DC-15 is labeled. The near N-S irregular cyan line shows the location of the Columbia River. (b) Cross-section B-B', a view from the NE—the dip direction of the thrust fault. The red error bar shows the estimated 95% uncertainty for the depth of the bedding-plane fault. (c) Cross-section C-C', a view from the NW, the strike direction of the thrust fault. The red error bar is described in Figure 5b.

velocity of deformation transients [*Roland and McGuire*, 2009]. In this study the seismicity migrated at speeds that suggest the swarm was driven by fluid pore pressure rather than aseismic slip, whereas the modeled deformation field shows that the vast majority of the observed deformation requires aseismic slip. The geologic setting of our study area, however, is different from that of previous studies.

[14] We suggest that interbed sediments play a central role in the aseismic slip. At many depths within the Saddle Mountain Basalt and Wanapum Basalt members of the CRBG (Figure 7) are sediment interbeds that formed on top of individual basalt flows during pauses between eruptions. The underlying and more voluminous Grande Ronde Basalt member is largely devoid of sediment interbeds because of the high eruption rate during its emplacement. The interbed sediments are dominantly lacustrine silts and clays of variable areal extent [*Reidel et al.*, 2002]. Clay-rich water-saturated sediments are thixotropic [*Jiang and Mehta*, 1995; *Kerr et al.*, 1970], so either a pressure pulse or the seismicity could have induced thixotropy by stressing the interbed sediment layer beyond its yield strength or triggering a thixotropic transition during one of the largest earthquakes (M 3.0) in late February and early March. After transition the clay rich sediments would behave as a highly mobile fluid. We theorize that this transition point was reached in mid-March 2009, when the seismicity migrated about 0.5 km to the shallow thrust fault in about eight days (Figure 6). The eight day migration would then represent the characteristic time of momentum diffusion in a fluid that served as an effective lubricant and pressure

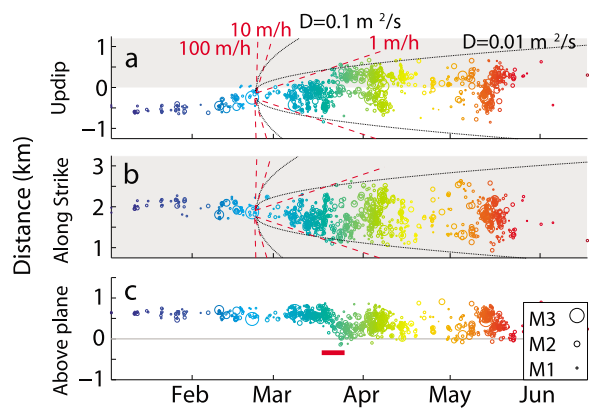

Figure 6. Earthquake migration relative to the thrust fault shown in Figure 5. (a) Earthquake migration with respect to the updip direction of the thrust fault plane. Earthquakes are scaled by magnitude and colored by time period (note that this color scheme is not the same as that used in Figure 5). Black dashed lines show the propagation of a pore pressure front given a hydraulic diffusivity (D) calculated relative to the location of the largest earthquake. Red dashed lines show migration rates from the largest earthquake. (b) Earthquake migration with respect to the strike direction. (c) Earthquake migration with respect to the distance above the fault plane. The horizontal red line shows the eight-day period of seismicity migration to the thrust fault surface.

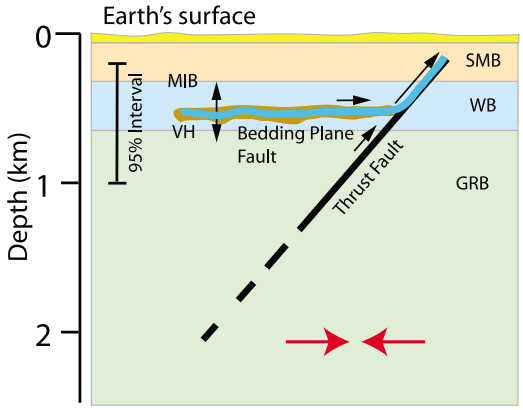

Figure 7. A schematic diagram that shows the relationship of the bedding-plane fault and the shallow thrust fault to local geology. The aseismic slip occurred on the two faults and the seismicity occurred in the underlying layers of basalt, between the two faults. We infer fluid involvement in the slip on the faults. The color-coded members of the CRBG are SMB, Saddle Mountains Basalt; WB, Wanapum Basalt; and GRB, Grande Ronde Basalt. The two major disconformities are VH (the Vantage Horizon) and MIB (the Mabton Interbed). The top yellow layer represents Upper Miocene to Quaternary deposits. The black error bars show the estimated 95% uncertainty for the depth of the bedding-plane fault, the same as shown in Figures 5b and 5c. The red arrows depict the near N-S tectonic convergence in the study area.

pulse facilitating aseismic slip. Using the characteristic distance of 0.5 km and characteristic time of eight days, we can make a useful estimate of the kinematic viscosity of the thixotropic fluid to be $\sim$0.36 $m^2\ s^{-1}$ (for reference, the kinematic viscosity of water is $\sim 1.14 \times 10^{-6}\ m^2\ s^{-1}$). The kinematic viscosity of thixotropic clay-rich sediments in mud volcanoes erupted from lower Miocene formations in Trinidad is $\sim$0.2–5 $m^2\ s^{-1}$ [*Kerr et al.*, 1970] similar to our estimate of kinematic viscosity for the interbed sediments. The depth and age of the Trinidad sediments are nearly the same as the depth and age of the CRBG interbed sediments. This model of aseismic slip is similar to viscous fault gouge models proposed to explain aseismic slip in Italy [*Bonafede et al.*, 1983; *Amoruso et al.*, 2004]. We expect that much of the slow updip and along-strike seismicity migration shown in Figure 6 is diffusion of the resultant pressure pulse similar to that observed in the 2000 Vogtland swarm [*Parotidis et al.*, 2003; *Hainzl and Ogata*, 2005].

[15] With the available data, we cannot say whether the seismicity or the aseismic slip started first. The seismicity or the aseismic slip (or perhaps both) might have been initiated by a pressure pulse resulting from a breached permeability barrier. Alternatively, the pulse could result from a surface process such as changing irrigation practices in the heavily developed agricultural areas east of and adjacent to the swarm, or from recent landslides on the bluffs of the nearby Columbia River. Seasonal groundwater recharge can result in pore pressure pulses capable of inducing seismicity at depths of $\sim$4.5 km [*Saar and Manga*, 2003] and induced seismicity within the upper three km of the crust has been shown to occur at several volcanic sites in the United States [*Christiansen et al.*, 2005].

[16] Candidates for the proposed bedding-plane fault include the Mabton Interbed (MIB) and the Vantage Horizon (VH) (Figure 7) and possible interbeds in between. In well DC-15 (Figures 2 and 5) the MIB is nearly 10 m thick. An interbed about 60 m deeper than the MIB has no sediments in DC-15 but about 6 m of sediments are present in a well 10 km to the NW. The VH is a major disconformity in the CRBG, representing a 250 ka pause in basalt eruptions [*Reidel et al.*, 2002]. The horizon contains a well-developed saprolite, and often sediments, but no associated sediments are found in well DC-15 (Figures 2 and 5). The MIB is the prime candidate for the bedding-plane fault for three reasons: (1) The thickness of the MIB is consistently near or greater than $\sim$10 m in DC-15 and surrounding wells, (2) the MIB has been shown to be a major detachment at the surface [*Reidel et al.*, 1994, and Reidel, personal communication, 2011], and (3) abundant core disking in well DC-15 begins at depths just below the MIB [*Landon*, 1985]. Core disking occurs where core samples break into near uniform thickness disks because of the introduction of transient stress changes in highly stressed rock during the drilling process [*Paillet and Kim*, 1987; *Lim et al.*, 2006]. Core disking is indicative of substantial horizontal stresses in the presence of high in situ stress that results from sufficient overburden (or depth) [*Lim et al.*, 2006]. There is no indication of core disking in the Saddle Mtn basalts (60–310 m depth) above the MIB in borehole DC-15 (Figures 2 and 5) [*Landon*, 1985]. Observations of core disking near 250 m depth in a well in Sweden [*Lim et al.*, 2006] suggest that the lower Saddle Mtn basalts are at a depth at which core disking can occur if the horizontal stress is sufficiently high. Below the MIB, from 320–475 m depth, about 5 m of the basalts in this depth range evidenced core disking. Core disking was common in the deeper basalts from 475 m to the total depth of 1293 m and it was prevalent in the flows with thicknesses of 30–120 m, where roughly 50%–75% of the basalt cores were disked. The presence of core disking below the MIB and lack of core disking above the MIB implies a change in the horizontal stress regime at the MIB with high horizontal stresses below the MIB and low horizontal stresses above the MIB.

5. Conclusion

[17] A recent aeromagnetic study [*Blakely et al.*, 2011] found that our modeled thrust fault is near, and strikes parallel to, the inferred axis of the Yakima Ridge anticline. We interpret the thrust fault to be part of a fold related thrust fault associated with the Yakima Ridge. It is probable that the entire fault length would be stressed but only the local section was weak enough to fail. Faults in the CRBG are the main natural pathways for vertical fluid migration [*Reidel et al.*, 2002]. Since the thixotropic sediments in Trinidad form sills and dikes at the surface [*Kerr et al.*, 1970], it is reasonable to suspect the presence of interbed sediments within the portion of the thrust fault that slipped aseismically. These sediments could have been introduced into the fault during past episodes of bedding-plane slip. In our interpretation it is the presence of these interbed sediments in the MIB and the shallow portion of the thrust fault

that enable the section of the CRBG above the MIB to slip thus relieving and preventing a substantial buildup of horizontal stresses. Below the MIB the thrust fault is not as free to move, because of the lack of intruded sediments, and because of the buildup of in situ horizontal stresses and thermal jointing, the rock is susceptible to microseismicity.

[18] The moment and duration of this event follow the scaling law for slow earthquakes proposed by *Ide et al.* [2007] where moment scales proportionally to the event duration time. The static stress drop [as defined by *Brodsky and Mori*, 2007) for our model ranges from 2 to 7 $\times$ 10^5 Pa, which is low for normal earthquakes and within the range of static stress drops for slow, or creep, events cataloged by *Brodsky and Mori* [2007]. However, if our model of aseismic slip involving clay-rich sediments is correct, the actual static stress drop is likely to be orders of magnitude smaller, putting this aseismic slip event into the low end of stress drops for slow events.

[19] **Acknowledgments.** This manuscript greatly benefited from reviews by Fred Pollitz, Jim Savage, Mitch Pitt, Steve Reidel, and an anonymous reviewer. We thank Steve Reidel for bringing the core disking and mapped MIB detachments to our attention. ENVISAT data were provided through ESA CAT-1 proposal 2765 and the WiNSAR Consortium (sponsored by NASA, NSF, and USGS).

References

Amoruso, A., L. Crescentini, M. Dragoni, and A. Piombo (2004), Fault slip controlled by gouge rheology: A model for slow earthquakes, *Geophys. J. Int.*, *159*, 347–352, doi:10.1111/j.1365-246X.2004.02386.x.

Beeler, N. M., and D. A. Lockner (2003), Why earthquakes correlate weakly with the solid Earth tides: Effects of periodic stress on the rate and probability of earthquakes, *J. Geophys. Res.*, *108*(B8), 2391, doi:10.1029/2001JB001518.

Blakely, R. J., B. L. Sherrod, C. S. Weaver, R. E. Wells, A. C. Rohay, E. A. Barnett, and N. E. Knepprath (2011), Connecting the Yakima fold and thrust belt to active faults in the Puget Lowland, Washington, *J. Geophys. Res.*, *116*, B07105, doi:10.1029/2010JB008091

Bonafede, M., E. Boschi, and M. Dragoni (1983), Viscoelastic stress relaxation on deep fault sections as a possible source of very long period elastic waves, *J. Geophys. Res.*, *88*, 2251–2260, doi:10.1029/JB088iB03p02251.

Bretz, J. H. (1925), The Spokane flood beyond the channeled scablands, *J. Geol.*, *33*, 97–115, doi:10.1086/623179.

Brodsky, E. E., and J. Mori (2007), Creep events slip less than ordinary earthquakes, *Geophys. Res. Lett.*, *34*, L16309, doi:10.1029/2007GL030917.

Brodtkorb, P. A., P. Johannesson, G. Lindgren, I. Rychlik, J. Rydén, and E. Sjö (2000), WAFO–a Matlab toolbox for analysis of random waves and loads, *Proc. ISOPE*, *3*, 343–350.

Christiansen, L. B., S. Hurwitz, M. O. Saar, S. E. Ingebritsen, and P. Hsieh (2005), Seasonal seismicity at western United States volcanic centers, *Earth Planet. Sci. Lett.*, *240*, 307–321, doi:10.1016/j.epsl.2005.09.012.

Cooke, M. L., and D. D. Pollard (1997), Bedding-plane slip in initial stages of fault-related folding, *J. Struct. Geol.*, *19*, 567–581, doi:10.1016/S0191-8141(96)00097-1.

Hainzl, S., and Y. Ogata (2005), Detecting fluid signals in seismicity data through statistical earthquake modeling, *J. Geophys. Res.*, *110*, B05S07, doi:10.1029/2004JB003247.

Ide, S., G. C. Beroza, D. R. Shelly, and T. Uchide (2007), A scaling law for slow earthquakes, *Nature*, *447*, 76–79, doi:10.1038/nature05780.

Jiang, F., and A. J. Mehta (1995), Mudbanks of the southwest coast of India IV: Mud viscoelastic properties, *J. Coastal Res.*, *11*, 918–926.

Jónsson, S. (2002), Modeling volcano and earthquake deformation from satellite radar interferometric observations, Ph.D. thesis, Stanford Univ., Palo Alto, Calif.

Jónsson, S., H. Zebker, P. Segall, and F. Amelung (2002), Fault slip distribution of the 1999 M_w 7.1 Hector Mine, California, earthquake, estimated from satellite radar and GPS measurements, *Bull. Seismol. Soc. Am.*, *92*, 1377–1389, doi:10.1785/0120000922.

Kerr, P. F., I. M. Drew, and D. S. Richardson (1970), Mud volcano clay, Trinidad, West Indies, *Am. Assoc. Pet. Geol. Bull.*, *54*, 2101–2110.

Landon, R. D. (1985), *Deep Borehole Stratigraphic Correlation Charts, SD-BWI-DP-035*, 257 pp., Rockwell Hanford Operations, Richland, Wash.

Lim, S. S., C. D. Martin, and R. Christiansson (2006), Estimating *in-situ* stress magnitudes from core disking, in *In-situ Rock Stress Measurement, Interpretation and Application*, edited by M. Lu et al., pp. 159–166, Taylor and Francis, London.

Lohman, R. B., and J. J. McGuire (2007), Earthquake swarms driven by aseismic creep in the Salton Trough, California, *J. Geophys. Res.*, *112*, B04405, doi:10.1029/2006JB004596.

Malone, S. D., G. H. Rothe, and S. W. Smith (1975), Details of microearthquake swarms in the Columbia Basin, Washington, *Bull. Seismol. Soc. Am.*, *65*, 855–864.

Mogi, K. (1967), Earthquakes and fractures, *Tectonophysics*, *5*, 35–55, doi:10.1016/0040-1951(67)90043-1.

Myrhaug, D., and H. Rue (1998), Joint distribution of successive wave periods revisited, *J. Ship Res.*, *42*, 199–206.

Okada, Y. (1985), Surface deformation due to shear and tensile faults in a half-space, *Bull. Seismol. Soc. Am.*, *75*, 1135–1154.

Paillet, F. L., and K. Kim (1987), Character and distribution of borehole breakouts and their relationship to in situ stresses in deep Columbia River basalts, *J. Geophys. Res.*, *92*, 6223–6234, doi:10.1029/JB092iB07p06223.

Parotidis, M., E. Rothert, and S. A. Shapiro (2003), Pore-pressure diffusion: A possible triggering mechanism for the earthquake swarms 2000 in Vogtland/NW-Bohemia, central Europe, *Geophys. Res. Lett.*, *30*(20), 2075, doi:10.1029/2003GL018110.

Peng, Z., and P. Zhao (2009), Migration of early aftershocks following the 2004 Parkfield earthquake, *Nat. Geosci.*, *2*, 877–881, doi:10.1038/ngeo697.

Philip, H., and M. Meghraoui (1983), Structural analysis and interpretation of the surface deformations of the El Asnam Earthquake of October 10, 1980, *Tectonics*, *2*, 17–49, doi:10.1029/TC002i001p00017.

Pitt, A. M. (1971), Micro-earthquake activity in the vicinity of Wooded Island, Hanford region, Washington, *U.S. Geol. Surv., Open File Rep.*, *72–298*, 24 pp.

Reidel, S. P., K. R. Fecht, M. C. Hagood, and T. L. Tolan (1989), The geologic evolution of the central Columbia Plateau, in *Volcanism and Tectonism in the Columbia River Flood-Basalt Province*, edited by S. P. Reidel and P. R. Hooper, *Geol. Soc. Am. Spec. Pap.*, *239*, 247–264.

Reidel, S. P., K. A. Lindsey, and K. R. Fecht (1992), *Field Trip Guide to the Hanford Site, WHC-MR-0391*, 50 pp., Westinghouse Hanford Co., Richland, Wash.

Reidel, S. P., N. P. Campbell, K. R. Fecht, and K. A. Lindsey (1994), Late Cenozoic structure and stratigraphy of southcentral Washington, in *Regional Geology of Washington State*, vol. 80, edited by E. Cheney and R. Lasmanis, pp. 159–180, Westinghouse Hanford Co., Richland, Wash.

Reidel, S. P., V. G. Johnson, and F. A. Spane (2002), Natural gas storage in basalt aquifers of the Columbia Basin, Pacific Northwest USA: A guide to site characterization, *Rep. PNNL-13962*, 277 pp., Pacific Northwest Nat. Lab., Richland, Wash.

Roland, E., and J. J. McGuire (2009), Earthquake swarms on transform faults, *Geophys. J. Int.*, *178*(3), 1677–1690, doi:10.1111/j.1365-246X.2009.04214.x.

Saar, M. O., and M. Manga (2003), Seismicity induced by seasonal groundwater recharge at Mt. Hood, Oregon, *Earth Planet. Sci. Lett.*, *214*, 605–618, doi:10.1016/S0012-821X(03)00418-7.

Simons, M., Y. Fialko, and L. Rivera (2002), Coseismic deformation from the 1999 M_w 7.1 Hector Mine, California, earthquake, as inferred from InSAR and GPS observations, *Bull. Seismol. Soc. Am.*, *92*, 1390–1402, doi:10.1785/0120000933.

Waitt, R. B., Jr. (1980), About 40 last-glacial Lake Missoula jökulhlaups through southern Washington, *J. Geol.*, *88*, 653–679, doi:10.1086/628553.

Waldhauser, F., and W. L. Ellsworth (2000), A double-difference earthquake location algorithm: Method and application to the Northern Hayward Fault, California, *Bull. Seismol. Soc. Am.*, *90*, 1353–1368, doi:10.1785/0120000006.

Wells, R. E., and R. W. Simpson (2001), Northward migration of the Cascadia forearc in the northwestern U.S. and implications for subduction deformation, *Earth Planets Space*, *53*, 275–283.

Yeats, R. S., K. E. Sieh, and C. R. Allen (1997), *Geology of Earthquakes*, Oxford Univ. Press, New York.

P. Bodin, Pacific Northwest Seismic Network, University of Washington, Seattle, WA 98195, USA.

J. Gomberg and C. Weaver, U. S. Geological Survey at Department of Earth and Space Sciences, University of Washington, Box 351310, Seattle, WA 98195, USA.

A. Rohay, Environmental Characterization and Risk Assessment Group, Pacific Northwest National Laboratory, Box 999, Richland, WA 99352, USA.

W. Thelen, U. S. Geological Survey, Cascades Volcano Observatory, 1300 SE Cardinal Ct., Bldg. 10, Ste. 100, Vancouver, WA 98683-9589, USA.

C. Wicks, U. S. Geological Survey, 345 Middlefield Rd. MS 977, Menlo Park, CA 94025, USA. (cwicks@usgs.gov)